Nuclear Materials and Energy 41 (2024) 101822

Contents lists available at ScienceDirect

Nuclear Materials and Energy

journal homepage: www.elsevier.com/locate/nme

Effective control of intrinsic impurities using n = 1 resonant magnetic perturbation (RMP) in EAST H-mode plasma

Wenmin Zhang [a,b], Ling Zhang [a,*], Shigeru Morita [c], Yunxin Cheng [a], Hui Sheng [a], Chengxi Zhou [a], Huihui Wang [a], Youwen Sun [a], Yuqi Chu [d], Ning Sun [a,b], Ailan Hu [a], Darío Mitnik [e], Yinxian Jie [a], Haiqing Liu [a]

[a] Institute of Plasma Physics, Hefei Institutes of Physical Science, Chinese Academy of Sciences, Hefei 230031, China
[b] University of Science and Technology of China, Hefei 230026, China
[c] National Institute for Fusion Science, Toki 509-5292, Gifu, Japan
[d] University of California Los Angeles, Los Angeles, CA 90095, USA
[e] Instituto de Astronomíay Física del Espacio (CONICET-Universidad de Buenos Aires), Buenos Aires 1428, Argentina

A R T I C L E I N F O

Keywords:
EAST plasma
Impurity screening layer
Impurity influx
Resonant magnetic perturbation

A B S T R A C T

Since 2021, EAST tokamak has been operated with full tungsten divertors. Tungsten accumulation has been frequently observed in NBI-heated H-mode discharges, resulting in the degradation of plasma confinement performance. Control of tungsten impurity is thus critical for the maintenance of high-confinement plasmas. In this work the impact of the $n = 1$ resonant magnetic perturbation (RMP) on the behavior of intrinsic low- and high-Z impurities in EAST H-mode discharges are experimentally studied, utilizing high-performance extreme ultraviolet spectroscopic diagnostics. In the dedicated discharge, ELM mitigation, ELM suppression, H-L back transition, RMP penetration occurs in succession with increasing RMP current (I_{RMP}). When I_{RMP} is below the threshold for H-L back transition, $I_{RMP\_H\text{-}L} = 2.29$ kA, increasing influx of C^{2+} and C^{3+} ions and decreasing influx of C^{4+} and C^{5+} ions are observed simutaneously with enhancement of the RMP field. This opposite time behavior in the influx of C^{4+} and C^{3+} ion is then observed to be magnified during the RMP penetration phase. It indicates a impurity screening layer formed between the locations where C^{4+} and C^{3+} ions distribute during RMP application based on our previous analysis (W.M. Zhang *et al* 2024 Nucl. Fusion 64 086004). A large step of increase in C^{4+} influx after H-L back transition indicates C^{4+} ion mainly located at bottom of pedestal. A higher RMP coil currents threshold capable of impurity screening is found for high-Z impurity ions of Cu^{25+}, Mo^{30+}, W^{42+}, i. e. 0.53–0.75 kA, than that for C^{4+} and C^{5+}, i. e. 0.33 kA. Meanwhile, it is found that comparing to C^{4+} and C^{5+} ions the decontamination effect by this impurity screening layer is more efficient for these high-Z impurity ions in plasma core region, e.g. up to 70 % reduction in the impurity density, leading to a significant reduction of radiation power. Furthermore, the continuous reduction of core high-Z impurities level both in ELM mitigation and suppression phase proved that this impurity decontamination effect by RMP field is dominant over the impact of ELM activity to core high-Z impurities transport since tungsten is frequently observed to accumulate during original ELM-free phase. Experimental results from this work would contribute to further understanding of the underlying mechanism how the RMP field impacts the impurity transport.

1. Introduction

Tungsten is adopted as the plasma-facing material (PFM) in magnetic-confinement devices due to its excellent material characteristic, such as high melting point, high energy threshold for sputtering and low tritium retention [1,2]. Very recently, instead of beryllium, tungsten is planned to be used as first wall material in addition to divertor targets in ITER. However, when plasma arrive at divertor target with high particle flux and heat flux, inevitable interaction between plasma and wall may cause transient or persistent tungsten sputtering. When the sputtered tungsten impurity penetrates through edge plasma and transports into high-temperature core plasma where they would be

* Corresponding author.
E-mail address: zhangling@ipp.ac.cn (L. Zhang).

https://doi.org/10.1016/j.nme.2024.101822
Received 5 July 2024; Received in revised form 6 November 2024; Accepted 20 November 2024
Available online 23 November 2024

ionized into highly charged tungsten impurity ions, resulting in large radiation power loss or triggering magnetohydrodynamic instability [3–5]. This degradation ultimately affects the performance of high-performance plasma, even cause radiation collapse and terminate discharge directly [6,7]. Therefore, control of tungsten impurity concentration in fusion plasmas is essential to improve energy confinement in magnetic-confinement devices. Several experimental approaches have been proved to be efficient to reduce the impurity concentrations in the plasma core, including on-axis electron cyclotron resonance heating [8,9] and lower-hybrid wave (LHW) heating [10–12], gas fueling [13], lithium and boron wall coating [14,15], and resonant magnetic perturbations (RMP) coils application [16,17]. Instability both in plasma edge and core region is proved to relieve core tungsten accumulation effectively, for example the edge localized mode (ELM) and sawtooth instability [11,12].

In high-confinement mode (H-mode) discharges, it has been demonstrated that RMP can effectivity mitigate and suppress ELM in several tokamaks, e.g. JET [18], ASDEX-Upgrade [19], KSTAR [20], MAST [21], DIII-D [22], and EAST [23]. In addition, the concentration of impurity ions in core plasma are clearly reduced during ELM mitigation and suppression phases demonstrating an effective impurity decontamination [23]. Previous studies have suggested that RMP field could reduce the impurity concentration through several mechanisms, such as reduction in impurity source generation due to ELM mitigation and suppression [24], enhanced impurity transport in the plasma edge by the neoclassical toroidal viscosity (NTV) and stochastic effect [25], and RMP field aiding in impurity screening in the pedestal [16]. However, the underlying physical mechanism remains uncertain.

Recently, the impact of $n = 1$ RMP field on impurity behaviour in EAST L-mode plasma was studied [26]. It was found that with the increase of RMP current (I_{RMP}), an impurity screening layer inside the last closed flux surface is formed. Outside this screening layer, the impurity ions influx gradually increase, while inside this screening layer, the impurity ions influx decrease gradually. The formation of impurity screening layer makes decontamination effect of impurities in the plasma core up to 60 %. Therefore, in this work, based on the observation of temporal evolution and spatial distribution of intrinsic impurity ions, the impact of impurity screening layer on low-Z impurity ions of carbon (C) and high-Z impurity ions of copper (Cu), molybdenum (Mo) and tungsten (W) in H-mode discharge is studied.

In the present paper, the experimental setup and the high-performance extreme ultraviolet (EUV) impurity spectroscopic diagnostic systems are described in section 2. The impact of RMP on the C, Cu and Mo impurity ions behaviour are presented in section 3. The effect of RMP on the core W impurity control is discussed in section 4. Finally, the work is summarized and discussed in section 5.

2. Experimental setup

The dedicated experiments were carried out in the EAST 2021 campaign. By 2021 both upper and lower divertor are equipped with tungsten-copper monoblock or flat tiles. Both the inboard and outboard side first wall is mainly composed of molybdenum tiles except for the inboard side area opposite to NBI port A and D remaining graphite tiles [26,27]. In addition, ion cyclotron resonance heating antennas and some diagnostic guard shielding are made by iron and copper materials. Due to the inevitable interaction between plasma and PFM, there are multiple impurity species in EAST plasma [27,28]. Two arrays of 8 flexible RMP saddle coils are toroidal symmetrically installed above and below the low-field-side midplane respectively in in-vessel EAST [29]. Each coil has four turns and could be operated at current up to 4.0 kA.

In order to monitor the time behavior of impurity ions in whole discharge and study on the edge-core coupling impurity transport, four fast-time-response (5 ms/frame) EUV spectrometers working in 5–500 Å called "EUV_Short", "EUV_Long_a", "EUV_Long_b" and "EUV_Long_c" [26,30], and a pair of space-resolved EUV spectrometers with time response of 200 ms/frame called "EUV_Long2_u" and "EUV_Long2_d", working in 30–520 Å (wavelength scanning) with different radial observation ranges of -6 cm $\leq Z \leq 44$ cm and -40 cm $\leq Z \leq 10$ cm at $R = 1.9$ m ($\rho \leq 0.7$) [31], have been developed on EAST. Furthermore, absolute intensity calibration has been performed to all EUV spectrometers by comparing the observed and calculated intensities of EUV bremsstrahlung continua [28]. Detailed performance of the spectrometers can be found in Ref. [26,30,31]. In the present study, in order to observe the temporal evolution of lower-ionized and highly ionized low-Z and high-Z impurities simultaneously, the fast-time-response EUV spectrometers of EUV_Short, EUV_Long_a, EUV_Long_b, and EUV_Long_c were operated at 5–50 Å, 40–180 Å, 245–500 Å, and 160–385 Å, respectively. The space-resolved EUV spectrometers were operated at 45–70 Å to measure the radial profiles of tungsten impurity ions. The influx of impurity ions entering the edge plasma is evaluated by the formula $\Gamma_i = I_{obs} \cdot S/XB$ [32], where Γ_i, I_{obs}, S, X and B denotes the impurity influx (ions•s^{-1}•m^{-2}), measured chord-integrated line intensity (photons·s^{-1}•m^{-2}), electron-impact ionization rate (s^{-1}·m^3), electron-impact excitation rate (s^{-1}·m^3) and the branching ratio, respectively. The S/XB values for $C^{2+} - C^{5+}$ are taken from the ADAS database [33].

In the experiment, the radial profiles of electron density (n_e) are measured by polarimeter interferometer (POINT) and reflectometry, and radial profiles of electron temperature (T_e) are provided by Thomson scattering (TS) and electron cyclotron emission (ECE) system. Radiation power loss are measured by fast-response bolometers (AXUV). Electron-scale turbulences with $k_\theta = 10$ cm^{-1} in the core plasma at $\rho \leq 0.4$ are observed by a CO_2 laser collective scattering system [34].

3. Effect of RMP on low- and high-Z impurity behaviour

In EAST NBI-dominant heating H-mode discharges with low safe factor of $q_{95} = 3.5$–4.2, the dependence of tungsten concentration in the core plasma, C_W, on ELM frequency, f_{ELM}, is statistically analysed, as shown in Fig. 1. The results show that without the application of RMP field ELMs with low frequents of $f_{ELM} = 20$–100 Hz appear and tungsten concentration is quite high, i.e. $C_W \sim 10^{-4}$. The tungsten accumulation has been often observed. In addition, as the discharge duration increases, the concentration of tungsten impurities continues to increase. When RMP filed is applied, tungsten concentration decreases significantly with increase of f_{ELM}. Simultaneously, it is found that the decontamination effect of RMP field with low toroidal mode number of $n = 1, 2$ on tungsten concentration seems to be better than that with high toroidal mode number of $n = 3, 4$. This may be related to the screening capability of the impurity screening layer and the radial position of the screening layer formed during the application of the RMP field.

A typical H-mode discharge of EAST #101787 with $n = 1$ RMP

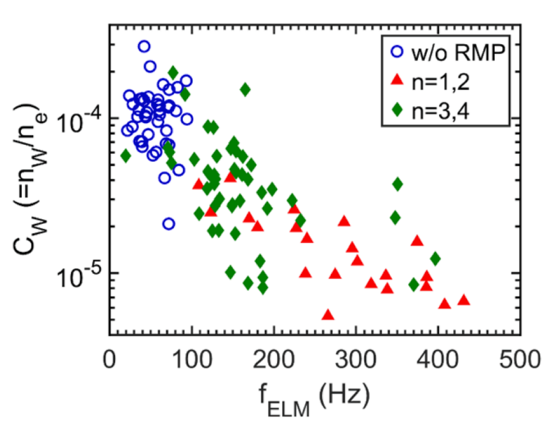

Fig. 1. Tungsten concentration in plasma core, C_W, as function of ELM frequency, f_{ELM}, with resonant magnetic perturbation (RMP) application (n: toroidal mode number of RMP) and comparison with non-RMP application in EAST NBI-dominant heating H-mode discharges.

current (I_{RMP}) ramp up is shown in Fig. 2. The plasma current I_p = 520 kA with flat top during t = 3.0–7.0 s, the toroidal field B_T = −2.3 T (clockwise from the top view), and upper single null (USN) configuration (unfavorable configuration). Plasma is heated by 4.65 GHz LHW with power of 1.5 MW from t = 1.5 s as well as NBI with power of 1.0 MW from t = 3.0 s, respectively (see Fig. 2(a)). As NBI switched on at t = 3.0 s, RMP coils start to be used until t = 6.5 s. It can be found that L-H transition occurs at t = 3.16 s quickly after injection of NBI (see D_α and stored energy (W_{MHD}) signals in Fig. 2(c)). During I_{RMP} ramp-up from 0 kA to 3.6 kA at t = 3.0–6.5 s, the amplitude of ELM, indicated by the D_α signal from the upper divertor, is mitigated during t = 3.6–4.5 s, and then is suppressed during t = 4.5–5.0 s. However, the grassy-ELM appears again during t = 5.0–5.26 s, which may be attributed to alterations in the pedestal structure induced by other electromagnetic perturbations. During the ELM mitigation and suppression, T_{e0} increases from 1.4 keV to 2.0 keV and n_e decrease from 3.7 × 10^{19} m^{-3} to 2.9 × 10^{19} m^{-3} gradually indicating a particle pump-out effect by RMP field (see Fig. 2(d)). Furthermore, the H-L back transition happens at 5.26 s ($I_{RMP\_H\text{-}L}$ = 2.29 kA). Fig. 2(e) shows that radiation in the plasma core (Core I_{AXUV}) increases during t = 3.0–3.7 s, and then gradually decreases, where transient sputtering events occur at t = 3.71 s, 3.99 s and 4.59 s resulting in an increase in core radiation. While radiation along the chord crossing plasma edge (Edge I_{AXUV}) indicate behaviors similar to ELM activity by D_α signal and meanwhile include an oscillated background intensity probably also due to ELM activity. The amplitude of core turbulence increases during ELM suppression compared to ELM mitigation in Fig. 2(f). The field penetration occurs at t = 6.0 s (I_{RMP_P} = 3.13 kA), where the radial magnetic response perturbations signal B_r (n = 1) suddenly increase (see Fig. 2(b)). It would be noted that the burst signal on the D_α from 6.0 s to 6.5 s is caused by plasma oscillation.

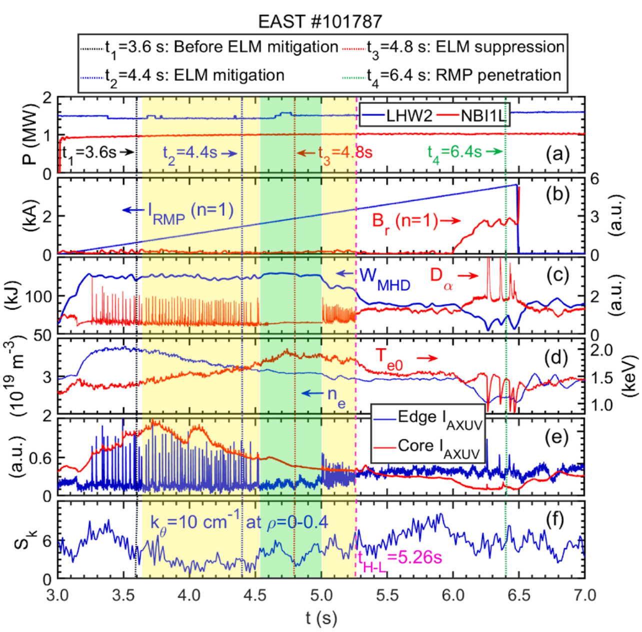

Fig. 2. Typical waveform of EAST #101787: LHW and NBI heating H-mode discharge with application of n = 1 RMP. Time evolution of (a) injected power of 4.65 GHz LHW, P_{LHW2} and NBI, P_{NBI1L}, (b) static n = 1 RMP coil currents, I_{RMP}, radial magnetic response perturbations, B_r, (c) plasma stored energy, W_{MHD} and D_α emission intensity, (d) line-averaged electron density, n_e and central electron temperature, T_{e0}, (e) radiation intensity along the chord mainly passing through plasma core, Core I_{AXUV} and edge, Edge I_{AXUV} and (f) turbulence amplitude with k_θ = 10 cm^{-1} at $\rho \le 0.4$. Time interval of ELM mitigation and suppression is indicated by light yellow and green shaded area, respectively. Vertical dotted lines at t = 3.6 s (black), 4.4 s (blue), 4.8 s (red), and 6.4 s (green) denote timings before ELM mitigation, during ELM mitigation, during ELM suppression, and during RMP penetration, respectively. The H-L transition occurs at 5.26 s indicated by magenta vertical dashed line. (For interpretation of the references to colour in this figure legend, the reader is referred to the web version of this article.)

In this discharge the n_e and T_e profiles at t_1 = 3.6 s before ELM mitigation, t_2 = 4.4 s during ELM mitigation, t_3 = 4.8 s during ELM suppression, and t_4 = 6.4 s during RMP penetration are shown in Fig. 3. Significant density pump-out effect during the ELM mitigation and suppression can be confirmed from the n_e profile measurement. At the former three timing peaked n_e profiles appears at least in $\rho \le 0.4$ (see Fig. 3(a)), while a flat n_e profile in large plasma range of $\rho \le 0.9$ is observed during field penetration phase. However, core T_e increases as density pumped out, i. e. by 180 eV and 470 eV during the phase of ELM mitigation and ELM suppression respectively. n_e and T_e profile at field penetration indicate a dramatically degraded plasma performance during this phase.

In order to study the effects of RMP on low-Z impurity behavior, C^{2+} – C^{5+} ions are selected due to relative stronger emission lines from these ions, it can be found from Fig. 2 that when the I_{RMP} is relatively small (I_{RMP} < 0.6 kA before t = 3.6 s), the RMP field strength is weak, and the impurity emission in the plasma core (Core I_{AXUV}) significantly increases due to good impurity confinement in H-mode. When I_{RMP} exceeds 0.6 kA, the RMP field begins to influence ELM activity, i.e. lead to decrease in ELM amplitude. Therefore, we analyze the changes in Γ_C^{Z+} with increasing I_{RMP} compared to I_{RMP} = 0.6 kA.

The change of normalized ion influx, $(\Gamma_C^{Z+})/(\Gamma_C^{Z+})\ I_{RMP}$ = 0.6 kA with I_{RMP} ramp-up for C^{2+} – C^{5+} is then illustrated in Fig. 4, where Z is the charge stage of C ion, and ionization energy interval for the ion of Z+, E_i = E_i (Z − 1)-E_i (Z), is also indicated. One may note that the behavior of carbon ions could be divided into two groups. With the enhancement of RMP field, on the one hand, the influx of C^{2+} (459.630 Å, E_i = 24–48 eV) and C^{3+} (384.180 Å, E_i = 48–64 eV) continue to increase. On the other hand, the influx of C^{4+} (40.268 Å, E_i = 64–392 eV) and C^{5+} (33.734 Å, E_i

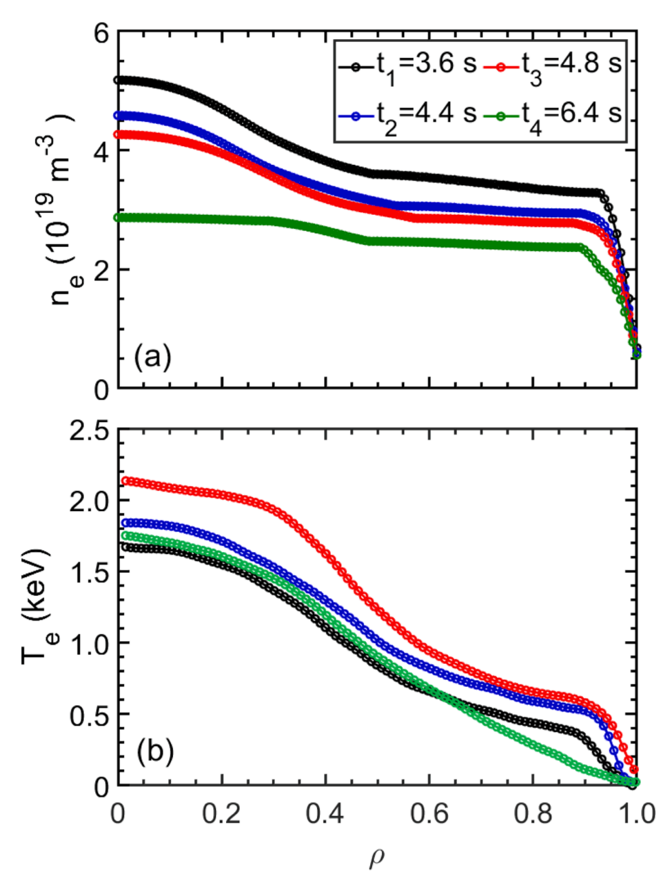

Fig. 3. Radial profiles of (a) electron density (n_e) and (b) electron temperate (T_e) at four timings of t_1-t_4 in EAST discharge #101787 indicated in Fig. 2.

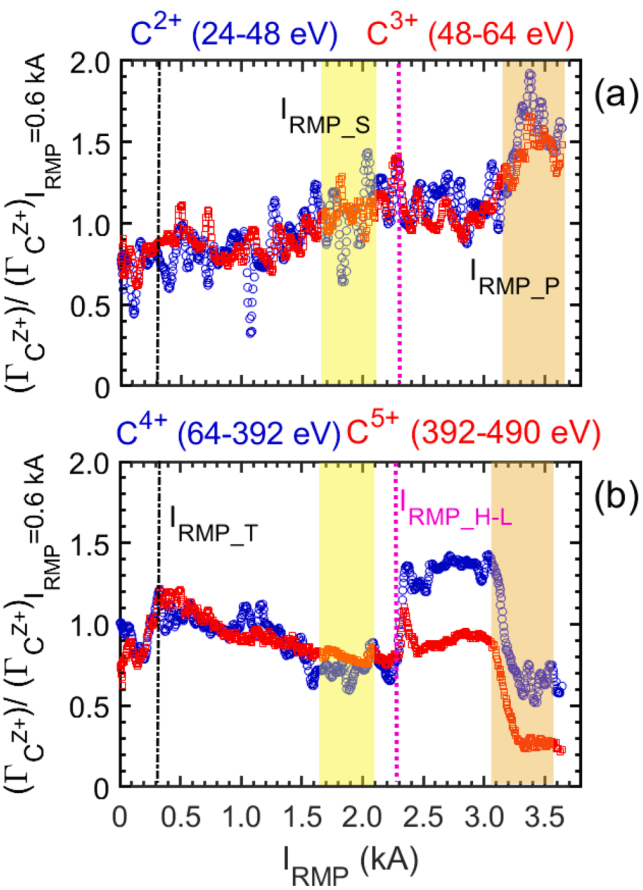

Fig. 4. Ratio of carbon ions flux with RMP field to that before ELM mitigation with $I_{RMP} = 0.6$ kA at $t = 3.6$ s, $(\Gamma_C^{Z+})/(\Gamma_C^{Z+})\ I_{RMP} = 0.6$ kA, as function of I_{RMP} for (a) C^{2+} (24–48 eV) from C III 459.630 Å and C^{3+} (48–64 eV) from C IV 384.180 Å, and (b) C^{4+} (64–392 eV) from C V 40.268 Å and C^{5+} (392–490 eV) from CVI 33.734 Å. Timing of threshold at $I_{RMP\_T} = 0.33$ kA, where C^{5+} influx begins to decrease, and H-L transition at $I_{RMP\_H\text{-}L} = 2.29$ kA is indicated by black and magenta line, respectively. Time interval of ELM suppression with $I_{RMP\_S} =$ 1.65–2.10 kA and of RMP penetration with $I_{RMP\_P} = 3.13$–3.60 kA are indicated by yellow and orange shaded area, respectively. (For interpretation of the references to colour in this figure legend, the reader is referred to the web version of this article.)

= 392–490 eV) ions continue to decrease at $I_{RMP} \geq 0.33$ kA, indicating a current threshold $I_{RMP\_T} = 0.33$ kA (black dotted line in Fig. 4) for core carbon impurity decontamination effect. A quick increase in C^{4+} and C^{5+} influx is observed at $I_{RMP} < 0.33$ kA probably due to enhanced plasma confinement. This opposite tendency between the influx of C^{2+} and C^{3+} and that of C^{4+} and C^{5+} ions suggest the formation of an impurity screening layer, based on our previous analysis [26], predominantly located between the locations of C^{3+} and C^{4+} ions distribution.

However, after the H-L back transition, there is a large step of increase in the influx ratio of C^{4+} and C^{5+} ions (see Fig. 4(b)), where the increase of C^{4+} influx ratio is three times of C^{5+} influx ratio. Simultaneously, the influx ratio of C^{2+} and C^{3+} ions (see Fig. 4(a)) almost keep constant. This suggests that C^{4+} and C^{5+} ions are primarily in the pedestal, with C^{4+} being closer to the foot of the pedestal while C^{2+} and C^{3+} ions are located completely outside the pedestal, i.e. in the scrape off layer (SOL) region. Since C^{2+} and C^{3+} ions are positioned beyond the impurity screening layer, they are practically unaffected by the crash of pedestal.

When the RMP field penetration occurs, the influx of C^{2+} and C^{3+} ions increase dramatically while that of C^{4+} and C^{5+} ions decrease significantly, suggesting the impurity screening layer still located between C^{3+} and C^{4+} ions. During this phase plasma performance is dramatically degraded (see blue lines in Fig. 2(c)) due to magnetic island formation at the $q = 2$ surface [26]. Comparing to ELM suppression phase, T_e decrease ~ 450 eV generally and the T_e pedestal already collapse in the field penetration phase (see red and green lines in Fig. 3 (b)), $C^{2+} - C^{5+}$ ions are then largely transport towards the plasma core region. Therefore, the location of impurity screening layer also shifted to the plasma core in this phase.

For a better understanding of carbon ions behavior under RMP filed in H-mode plasma, based on the time evolution of $C^{2+} - C^{5+}$ ions influx before and after the H-L back transition, radial position of carbon ions and that of the impurity screening layer are roughly estimated referring to the ion ionization energy and the determined pedestal region from T_e profile during ELM suppression. As illustrated in Fig. 5(a), during ELM suppression phase C^{5+} ion is located in the pedestal and closed to the pedestal top, and C^{4+} ion is closed to the pedestal foot, while C^{3+} and C^{2+} ion is located completely outside the pedestal region. Meanwhile, the impurity screening layer is mainly located between C^{4+} and C^{3+}, e.g., in the SOL. Following RMP penetration, the impurity screening layer moves toward the plasma core and (see Fig. 5(b)). It is note that the spatial distribution of carbon ions is derived using spline interpolation method [26], based on the spatial distribution of W^{26+} at 49.0 Å ions measured by space-resolved EUV spectrometer. This method is described in detail in [26].

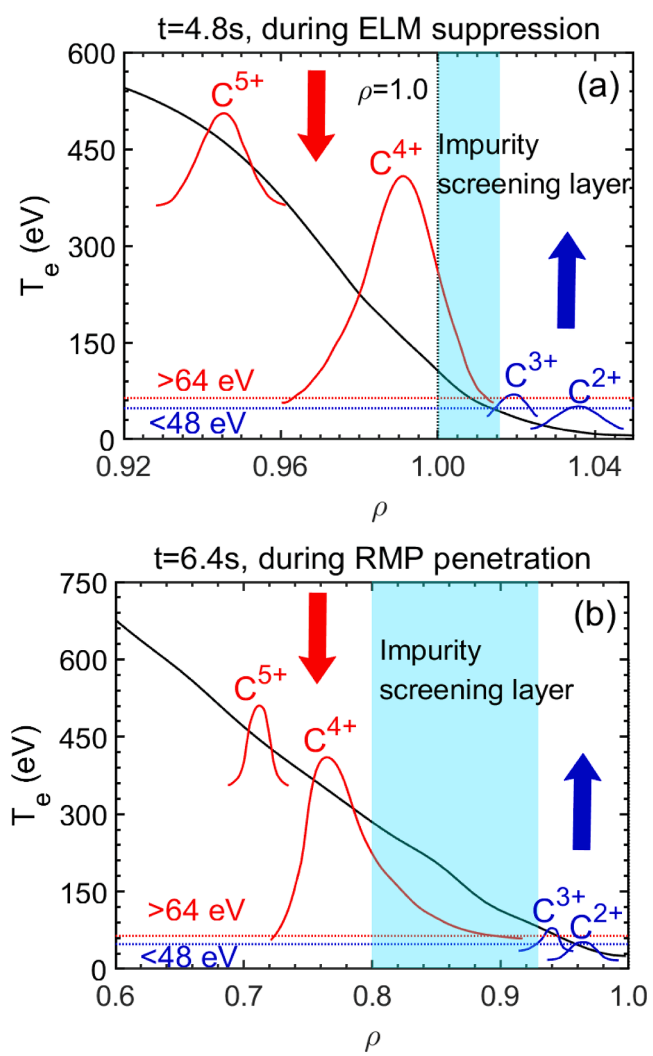

Fig. 5. Estimation of the radial position of impurity screening layer (cyan shaded area) during (a) ELM suppression and (b) RMP penetration. (For interpretation of the references to colour in this figure legend, the reader is referred to the web version of this article.)

The decontamination effect of RMP field strength on high-Z impurities of Mo^{30+} (1587–1730 eV), W^{42+} (1995–2149 eV) and Cu^{25+} (2307–2479 eV) are illustrated in Fig. 6, which is derived from line emission of Mo XXXI at 115.999 Å, W XLIII at 47.191 Å and Cu XXVI at 111.186 Å respectively. It is noted that W peak at $I_{RMP} = 1.05$ kA ($t = 4.03$ s) may be due to an intensity increase following a sudden edge W burst (see Fig. 2(e)). A threshold current of $I_{RMP\_T} \sim 0.53$–0.75 kA (green shaded area) is observed for high-Z impurity decontamination, which is similar to that for core I_{AXUV} decreasing due to high-Z impurities predominantly contributing to the plasma core radiation. As the I_{RMP} increases from 1.25 kA to 2.29 kA during the ELM mitigation and suppression phase, there is a significant decrease in the impurity ion flux, resulting in the decontamination effect of 30 %-70 %. In addition, the decontamination effect does not appear to be notably influenced by the impurity atomic number, for example both Mo and Cu show similar decontamination effects. Furthermore, when H-L back transitions or even RMP penetration occurs, the core impurity decontamination effect is further enhanced due to the degradation of the plasma confinement performance.

4. Effect of RMP on tungsten impurity control

Vertical profiles of chord-integrated intensity for W^{26+} (784–833 eV) at 49.0 Å, W^{32+} (1283–1335 eV) at 52.200 Å, W^{38+} (1622–1830 eV) at 63.883 Å, and W^{42+} (1995–2149 eV) at 47.191 Å ($\rho < 0.7$) ions in EAST discharge #101787 at four timings spectrometer are shown in Fig. 7. Before ELM mitigation, the peak position of W^{26+}, W^{32+}, W^{38+} and W^{42+} are $\rho = 0.22$, 0.16, 0.08 and 0, respectively. During the application of RMP field, with the formation of impurity screening layer, W impurity radiation markedly diminishes and flattens. After ELM suppression, the decontamination effect for tungsten impurity ions can reach to 70 %. These findings highlight that the application of the RMP field effectively suppresses tungsten impurity accumulation and reduces the concentration of tungsten impurity in the plasma core. When H-L back transition occurs and RMP penetration happens, due to the degradation of plasma confinement performance, the tungsten impurity content decreases to extremely low levels and approaches zero.

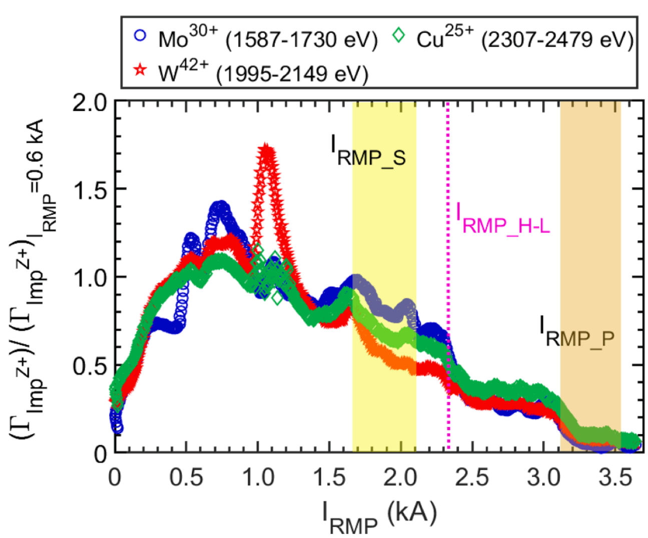

Fig. 6. Ratio of high-Z impurity ions influx with RMP field to that before ELM mitigation with $I_{RMP} = 0.6$ kA at $t = 3.6$ s, $(\Gamma^{Z+}_{Imp})/(\Gamma^{Z+}_{Imp})\ I_{RMP} = 0.6$ kA, as function of I_{RMP} for Mo^{30+} (1587–1730 eV) from Mo XXXI 115.999 Å, W^{42+} (1995–2149 eV) from W XLIII 47.191 Å, and Cu^{25+} (2307–2479 eV) from Cu XXVI 111.186 Å. Time interval for threshold with $I_{RMP\_T} = 0.53$–0.75 kA where the influx begin to decrease is indicated by green shaded area. Indication of time interval of ELM suppression and RMP penetration and the timing at H-L back transition are the same as in Fig. 4. (For interpretation of the references to colour in this figure legend, the reader is referred to the web version of this article.)

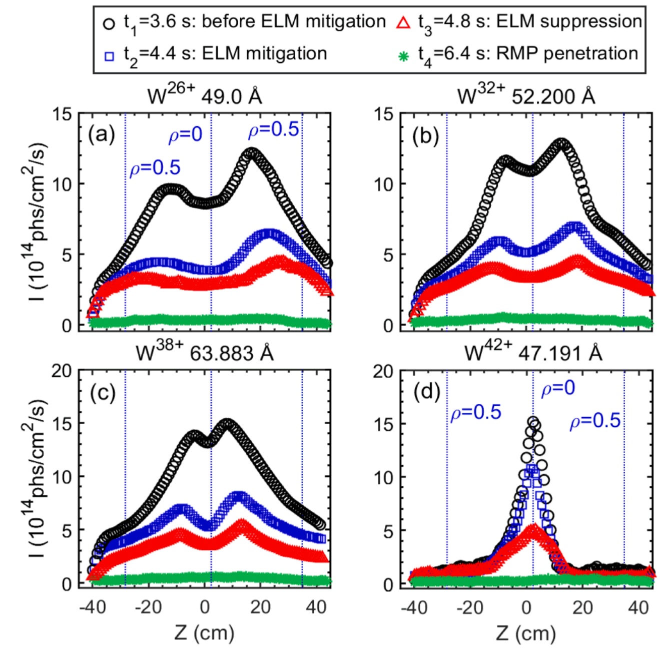

Fig. 7. Vertical intensity profiles of tungsten lines from different charge states: (a) W^{26+} (784–833 eV) from W XXVII 49.0 Å, (b) W^{32+} (1283–1335 eV) from W XXXIII 52.200 Å, and (c) W^{38+} (1622–1830 eV) from W XXXIX 63.883 Å, and (d) W^{42+} (1995–2149 eV) from W XLIII 47.191 Å at four timings of t_1-t_4 indicated in Fig. 2. Radial locations of $\rho = 0$ and 0.5 are indicated with blue dotted lines. (For interpretation of the references to colour in this figure legend, the reader is referred to the web version of this article.)

5. Discussion and conclusion

In EAST NBI-dominant heating H-mode discharges with relatively low q_{95} (3.5–4.2), the statistical results show that with application of RMP coils, the C_W in the plasma core decreases with the increase of f_{ELM}, indicating a synthetic effect of ELM mitigation and tungsten control by RMP fields. It is proved that tungsten decontamination effect with low n ($n = 1$, 2) is better than that with high n ($n = 3$, 4). A dedicated experiment is therefore executed to study the process of impurity behaviour and understand the underlying physics mechanism.

When both NBI power and RMP fields are applied simultaneously, at low RMP field strengths, the influx of impurity ions in the plasma core increases gradually with the ramp-up of I_{RMP}. Once I_{RMP} exceeds a certain threshold, the influx of these impurity ions gradually declines. For low-Z impurity (C), this threshold current is 0.33 kA, whereas for high-Z impurities (Cu, Mo, W), it varies between 0.53 kA and 0.75 kA. Therefore, with the ramp-up of I_{RMP} during ELM mitigation and suppression and RMP penetration phase, the influx of C^{2+} and C^{3+} ions increase while that of C^{4+} and C^{5+} ions decrease significantly. This suggests the formation of a radial impurity screening layer, consistently positioned between C^{4+} and C^{3+} ions. Following the H-L transition, the influx of C^{2+} and C^{3+} ions keep constant, while there is a jump step of increase in the influx of C^{4+} and C^{5+} ions, with the increase in C^{4+} being three times that of C^{5+}. This indicates that C^{2+} and C^{3+} ions are predominantly located in the SOL, whereas C^{4+} and C^{5+} ions are mainly found in the pedestal, particularly C^{4+} ions are estimated to be closer to the pedestal foot. The impurity screening layer is primarily situated in the SOL region.

The impurity screening layer is more effective in reducing impurity concentration in the plasma core for high-Z impurity ions, i.e. Cu^{25+}, Mo^{30+}, $W^{26+} - W^{42+}$, compared to C^{4+} and C^{5+} ions. Up to 70 % of reductions in impurity density is observed, which results in a significant decrease in radiation power. Furthermore, the continual decrease in core high-Z impurity levels during both ELM mitigation and suppression phases indicates that the impurity decontamination effect by RMP fields dominant over the impact of ELM activity on high-Z impurity transport because high-Z impurities of tungsten are frequently observed to accumulate during original ELM-free phases. In addition, the spatial distribution of W^{26+}, W^{32+}, W^{38+}, and W^{42+} ions also show the consistent temporal and spatial evolution behaviour.

After the H-L back transition, a jump step of increase in the influx of C^{4+} and C^{5+} ions are observed. Meanwhile, the influx of high-Z impurity ions into the plasma core continues to decrease. This behavior can likely be attributed to the expulsion of impurity ions from the plasma core after the collapse of the edge transport barrier. These expelled impurity ions undergo recombination with electrons in lower-temperature regions, transitioning to a lower-ionized state. Due to the impurity screening layer, these lower-ionized stage ions accumulate near this layer, resulting in a significant increase in their flux.

Due to the limitation of coverage in plasma edge by the space-resolved EUV spectrometers, e.g. $\rho > 0.7$, it is difficult to observe the full spatial distribution of $C^{2+} - C^{5+}$ ions which peaked at the plasma edge. At present, a newly developed visible spectrometer covering the entire poloidal section just started to be operated, which is expected to enhance the observation of the spatial distribution of weekly ionized impurity ions at the plasma edge, e.g. for C^{+} at 513.92 nm, C^{2+} at 465.02 nm, and C^{4+} at 227 nm. It will greatly help to exactly determine the location of the impurity screening layer and study the edge impurity transport. In the future work, the weekly ionized tungsten impurity ions of $W^{4+} - W^{8+}$, which are newly identified from EAST plasma, will also be used to study the edge tungsten impurity transport during the application of RMP fields.

CRediT authorship contribution statement

Wenmin Zhang: Writing - review & editing, Writing - original draft, Investigation, Formal analysis, Data curation. **Ling Zhang:** Writing-review & editing, Supervision, Project administration, Investigation, Formal analysis. **Shigeru Morita:** Methodology, Formal analysis, Investigation. **Yunxin Cheng:** Investigation, Data curation. **Hui Sheng:** Investigation, Data curation. **Chengxi Zhou:** Investigation, Data curation. **Huihui Wang:** Investigation, Data curation. **Youwen Sun:** Investigation, Data curation. **Yuqi Chu:** Investigation, Data curation. **Ning Sun:** Investigation, Data curation. **Ailan Hu:** Data curation. **Dario Mitnik:** Data curation. **Yinxian Jie:** Supervision, Data curation. **Haiqing Liu:** Supervision, Data curation.

Declaration of competing interest

The authors declare that they have no known competing financial interests or personal relationships that could have appeared to influence the work reported in this paper.

Acknowledgements

This work was supported by the National Magnetic Confinement Fusion Energy R&D Program of China (Grant No. 2022YFE03180400), National Natural Science Foundation of China (Grant No. 12322512) and Chinese Academy of Sciences President's International Fellowship Initiative (PIFI) (Grant Nos. 2025PVA0060, 2024PVA0074),.

Data availability

Data will be made available on request.

References

[1] T. Hirai, et al., Use of tungsten material for the ITER divertor, *Nucl. Mater. Energy* 9 (2016) 616–622.
[2] V. Philipps, et al., Tungsten as material for plasma-facing components in fusion devices, *J. Nucl. Mater.* 415 (2011) S2–S9.
[3] T. Pütterich, et al., Determination of the tolerable impurity concentrations in a fusion reactor using a consistent set of cooling factors, *Nucl. Fusion* 59 (2019) 056013.
[4] H.E. Ferrari, et al., The effect of a saturated kink on the dynamics of tungsten impurities in the plasma core, *Plasma Phys. Control. Fusion* 61 (2019) 035010.
[5] S.S. Pan, et al., Observation of tearing mode triggering by sawtooth crash with high-Z impurity accumulation in EAST, *AIP Adv.* 13 (2023) 045108.
[6] I. Nunes, et al., Plasma confinement at JET, *Plasma Phys. Control. Fusion* 58 (2016) 014034.
[7] K.H. Burrell, et al., Confinement physics of H-mode discharges in DIII-D, *Plasma Phys. Control. Fusion* 31 (1989) 1649.
[8] Y.C. Shen, et al., Suppression of molybdenum impurity accumulation in the core using on-axis electron cyclotron resonance heating in EAST, *Phys. Plasmas* 26 (2019) 032507.
[9] C. Angioni, et al., A comparison of the impact of central ECRH and central ICRH on the tungsten behaviour in ASDEX Upgrade H-mode plasmas, *Nucl. Fusion* 57 (2017) 056015.
[10] L. Zhang, et al., Suppression of tungsten accumulation during ELMy H-mode by lower hybrid wave heating in the EAST tokamak, *Nucl. Mater. Energy* 12 (2017) 774–778.
[11] M. Sertoli, et al., Interplay between central ECRH and saturated (m, n)=(1, 1) MHD activity in mitigating tungsten accumulation at ASDEX Upgrade, *Nucl. Fusion* 55 (2015) 113029.
[12] T.C. Hender, et al., The role of MHD in causing impurity peaking in JET hybrid plasmas, *Nucl. Fusion* 56 (2016) 066002.
[13] E. Joffrin, et al., First scenario development with the JET new ITER-like wall, *Nucl. Fusion* 54 (2013) 013011.
[14] W. Xu, et al., Comparison of active impurity control between lithium and boron powder real-time injection in EAST, *Phys. Scr.* 96 (2021) 124034.
[15] A. Kallenbach, et al., Overview of ASDEX Upgrade results, *Nucl. Fusion* 57 (2017) 102015.
[16] B.S. Victor, et al., Impurity transport in the pedestal of H-mode plasmas with resonant magnetic perturbations, *Plasma Phys. Control. Fusion* 62 (2020) 095021.
[17] E.T. Hinson, et al., Enhanced helium exhaust during edge-localized mode suppression by resonant magnetic perturbations at DIII-D, *Nucl. Fusion* 60 (2020) 054004.
[18] Y.F. Liang, et al., Active control of type-I edge-localized modes with n= 1 perturbation fields in the JET tokamak, *Phys. Rev. Lett.* 98 (2007) 265004.
[19] W. Suttrop, et al., Experimental conditions to suppress edge localised modes by magnetic perturbations in the ASDEX Upgrade tokamak, *Nucl. Fusion* 58 (2018) 096031.
[20] I. Yongkyoon, et al., Test of the ITER-like resonant magnetic perturbation configurations for edge-localized mode crash suppression on KSTAR, *Nucl. Fusion* 59 (2019) 126045.
[21] A. Kirk, et al., Resonant magnetic perturbation experiments on MAST using external and internal coils for ELM control, *Nucl. Fusion* 50 (2010) 034008.
[22] T.E. Evans, et al., Suppression of large edge localized modes in high confinement DIII-D plasmas with a stochastic magnetic boundary, *Phys. Rev. Lett.* 92 (2004) 235003.
[23] Y.W. Sun, et al., First demonstration of full ELM suppression in low input torque plasmas to support ITER research plan using n= 4 RMP in EAST, *Nucl. Fusion* 61 (2021) 106037.
[24] X.H. Chen, et al., The impact of ELM mitigation on tungsten source in the EAST divertor, *Nucl. Fusion* 61 (2021) 046046.
[25] Y.Y. Chang, et al., Tungsten transport due to the neoclassical toroidal viscosity induced by resonant magnetic perturbation in the EAST tokamak, *Phys. Plasmas* 30 (2023) 122301.
[26] W.M. Zhang, et al., First observation of edge impurity behavior with n = 1 RMP application in EAST L-mode plasma, *Nucl. Fusion* 64 (2024) 086004.
[27] W.M. Zhang, et al., Line identification of extreme ultraviolet (EUV) spectra from iron, copper and molybdenum ions in EAST tokamak, *Phys. Scr.* 97 (2022) 045604.
[28] L. Li, et al., Line identification of extreme ultraviolet (EUV) spectra from low-Z impurity ions in EAST tokamak plasmas, *Plasma Sci. Technol.* 23 (2021) 075102.
[29] Y.W. Sun, et al., Edge localized mode control using n= 1 resonant magnetic perturbation in the EAST tokamak, *Nucl. Fusion* 57 (2016) 036007.
[30] W.M. Zhang, et al., Spectroscopic analysis of tungsten spectra in extreme-ultraviolet range of 10-480 Å observed from EAST tokamak with full tungsten divertor, *Phys. Scr.* 99 (2024) 105609.
[31] Y.X. Cheng, et al., Performance improvement of space-resolved extreme ultraviolet spectrometer by use of complementary metal-oxide semiconductor detectors at the Experimental Advanced Superconducting Tokamak, *Rev. Sci. Instrum* 93 (2022) 123501.
[32] K. Behringer, et al., Spectroscopic determination of impurity influx from localized surfaces, *Plasma Phys. Control. Fusion* 31 (1989) 2059.
[33] The Atomic Data and Analysis Structure (ADAS) is an Interconnected Set of Computer Codes and Data Collections for Modelling the Radiating Properties of Ions and Atoms in Plasmas. [Online]. Available: https://open.adas.ac.uk/.
[34] P. Li, et al., Study of turbulence modulation and core density peaking with CO_2 laser collective scattering diagnostics in the EAST tokamak, *Nucl. Fusion* 60 (2020) 066001.